Adsorption-Coupled Electron-Transfer Mode of Scanning Electrochemical Microscopy: Voltammetric Simulation

Donald C. Janda,[a] Kiran Barma,[a,b] Moghitha Parandhaman,[a] Xindi Sun,[a] Kevin C. Leonard,[c] and Shigeru Amemiya[a,*]

[a] Department of Chemistry, University of Pittsburgh, 219 Parkman Avenue, Pittsburgh, Pennsylvania, 15260, United States

[b] UM-DAE, Centre for Excellence in Basic Sciences, University of Mumbai, Mumbai, 400098, India

[c] Center for Environmentally Beneficial Catalysis, Department of Chemical and Petroleum Engineering, University of Kansas, 1501 Wakarusa Drive, Lawrence, Kansas 66047, United States

* To whom all correspondence should be addressed. E-mail: amemiya@pitt.edu. Fax : 412-624-8611.

Keywords: Adsorption-coupled electron transfer, Scanning electrochemical microscopy, Kinetic zone diagram, COMSOL Multiphysics

Abstract

The coupling between the electron transfer and specific adsorption of a redox-active molecule is ubiquitous and crucial in many important electrode reactions. Practically, adsorption-coupled electron-transfer (ACET) reactions generate irreversibly adsorbed products in electrodeposition and electrointercalation and reversibly adsorbed intermediates in electrocatalysis and photoelectrocatalysis. Fundamentally, ACET reactions are highly complex owing to the co-existence of concerted and non-concerted mechanisms. Herein, we model the ACET mode of scanning electrochemical microscopy (SECM) theoretically to experimentally and quantitatively investigate the dynamics and mechanism of ACET reactions. Specifically, an ACET reaction at the substrate is driven voltammetrically and monitored amperimentrically at the tip to yield the voltammogram of the tip current versus the cycled substrate potential. In the negative ACET mode, irreversible adsorbates are produced from reversibly adsorbed reactants through the concerted or non-concerted mechanism. Moreover, reversible adsorbates are produced from non-adsorbing reactants through the concerted or non-concerted mechanism in the positive ACET or positive feedback mode, respectively, as complemented by the substrate generation/tip collection mode of both mechanisms. We predict that the ACET mechanism can be identified when a reversible adsorption step is kinetically controlled. The validity and application of our model are demonstrated by considering various substrate reactions reported previously. These reactions include hydrogen electrocatalysis, metal electrodeposition, lithium electrointercalation, the ACET-like formation of metal oxides, and even the redox reaction of a conducting polymer coupled with ion transfer. The powerful ACET mode will complement the surface-interrogation mode based on the quantitation of preformed adsorbates.

1. Introduction

Many important electrode reactions involve the coupling between the electron transfer (ET) and specific adsorption of a redox-active species [1, 2] to represent adsorption-coupled electron-transfer (ACET) reactions [3]. Electrodeposition [4] and electrointercalation [5] exemplify ACET reactions as

$$O + M + e \rightleftharpoons R_{ads} \quad (1)$$

where O is an oxidant in the solution, R_{ads} is the reductant adsorbed on the electrode surface, e.g., a metal ion and an irreversibly adsorbed metal atom, respectively, and M is an adsorption site. Moreover, ACET reactions are ubiquitous and crucial in electrocatalysis [1, 6, 7] and photoelectrocatalysis [1] to produce an adsorbed intermediate, which can be reversibly desorbed to form a soluble reductant, R, as

$$R + M \rightleftharpoons R_{ads} \quad (2)$$

For instance, both adsorbed and non-adsorbed forms of $O_2^{\bullet-}$ [8, 9] and $CO_2^{\bullet-}$ [10, 11] were detected experimentally as the key intermediates of electrochemical O_2 [12, 13] and CO_2 [14, 15] reduction reactions, respectively.

Fundamentally, the molecular mechanism of ACET reactions is highly complicated [1] and ambiguous owing to the co-existence of concerted and non-concerted mechanisms [2, 3, 16-18]. The ACET reaction of an irreversible adsorbate can be mediated through the concerted mechanism (Equation 1) as well as the non-concerted mechanism based on separate adsorption and inner-sphere ET steps [2, 3, 16, 18]

$$O + M \rightleftharpoons O_{ads} \quad (3)$$

$$O_{ads} + e \rightleftharpoons R_{ads} \quad (4)$$

The non-concerted mechanism was predicted theoretically to account for the fast electrodeposition of silver [19] and hydrogen [20] but has not been resolved from the concerted mechanism experimentally [3, 18]. The reversibly adsorbed intermediate of electrocatalysis and photoelectrocatalysis can be

produced through the non-concerted mechanism [2, 3, 16, 17], where the adsorption step (Equation 2) is preceded by the outer-sphere ET step

$$O + e \rightleftharpoons R \tag{5}$$

The rate and final product of gross catalytic reactions strongly depend on the reaction mechanism [12-15].

Herein, we develop the voltammetric theory for the ACET mode of scanning electrochemical microscopy (SECM) to quantitatively investigate the dynamics and mechanism of ACET reactions. Specifically, an ACET reaction at the substrate is driven voltammetrically and monitored amperometrically at the tip to measure the tip current against the cycled substrate potential [21, 22]. In the negative ACET mode, irreversible adsorbates are produced from non-adsorbed reactants (Figure 1A) or reversibly adsorbed reactants through concerted and non-concerted mechanisms to lower the tip current without the substrate reaction at the initial potential [21, 22]. In the positive ACET mode, reversible adsorbates are produced at the tip to regenerate non-adsorbed reactants at the substrate, thereby enhancing the tip current [23] (Figure 1B). The positive ACET mode of the concerted mechanism is distinct from the positive feedback mode of the non-concerted mechanism and complemented by the substrate generation/tip collection (SG/TC) mode of both mechanisms [24]. When the reversible adsorption step is kinetically controlled, unique voltammograms are expected for each mechanism to discriminate between the two mechanisms [2, 3, 24].

More broadly, we generalize the theory of SECM-based voltammetry [25] to understand ACET reactions at the substrate more quantitatively than reported in the previous experimental work. Advantageously, we consider transient voltammetric conditions to manifest adsorption effects, which are concealed by employing SECM under steady-state conditions [26]. Specifically, the theoretical voltammograms of the negative ACET mode simulate experimental voltammograms for the

underpotential deposition of hydrogen [21, 22, 27], the ACET-like formation of metal oxides [22], and lithium electrointercalation [28]. Moreover, the voltammograms predicted for the negative ACET mode manifest that the redox reaction of a conducting polymer film can be concerted or non-concerted with ion transfer [29-32]. Furthermore, we compare positive ACET and positive feedback modes to identify non-concerted and concerted mechanisms for the ACET reaction of ferrocene derivatives [24] and the hydrogen oxidation reaction [23], respectively. We also assess the experimental voltammogram of copper electrodeposition in the SG/TC mode [33]. Finally, the ACET mode is compared with the surface-interrogation (SI) mode based on the quantitation of adsorbates preformed through ACET or ACET-like reactions [34].

2. Results and Discussion

2.1. Diffusion-reaction model

The diffusion-reaction model of ACET reactions was developed and validated for cyclic voltammetry (CV) [2, 3] and SECM [24] and generalized in this work (see Supplementary Materials). The generalized model was solved numerically by employing the finite element method in COMSOL Multiphysics (version 6.0, COMSOL, Burlington, MA). A few hundred voltammograms were obtained for each kinetic zone diagram and analyzed by using home-written Python and Java programs. Specifically, the diffusion-reaction model was extended to the negative ACET mode to discriminate between concerted and non-concerted mechanisms. The respective mechanisms were considered for positive ACET and positive feedback modes as complimented by the SG/TC mode to simulate more general conditions than reported in our recent work [24]. The tip–substrate distance, d, was added to the diffusion-reaction model of SECM in comparison with that of CV. We selected a sufficiently short tip–substrate distance of $d/a = 0.5$, where a represents the inner radius of the tip. The outer radius of the tip,

r_g, was also fixed to $RG = r_g/a = 2.0$. In addition, the scan rate of the substrate potential, v, was normalized against the inner tip radius to yield

$$\sigma = \frac{a^2 vF}{DRT} \tag{6}$$

where the diffusion coefficients of the oxidant and reductant are both assumed to be D. We selected $\sigma = 0.15$ to represent typical experimental conditions of $v = 0.1$ V/s and 10 V/s for $a = 5$ μm and 0.5 μm, respectively, in Equation 6 with $D = 7 \times 10^{-6}$ cm^2/s.

An ACET reaction at the substrate was characterized by two dimensionless parameters. A dimensionless parameter, κ, represented the ratio of the total concentration of adsorption sites at the substrate, Γ_s, against the availability of the oxidant within the diffusion layer near the substrate as given by

$$\kappa = \frac{\Gamma_s}{c_0}\sqrt{\frac{Fv}{RTD}} \tag{7}$$

where c_0 is the concentration of the oxidant in the solution. For instance, κ increases with higher v or lower c_0 to enhance the adsorption effect from the ACET reaction as well as the adsorption step. In addition, the standard rate constant of the ACET reaction was given in the dimensionless form, Λ_C^O, by

$$\Lambda_C^O = k_C^O\sqrt{c_0 c_{st}}\frac{RT}{\Gamma_s Fv} \tag{8}$$

where c_{st} is a standard concentration, e.g., 1 M. The standard rate constants of outer-sphere and inner-sphere ET steps were also defined in the dimensionless form (see Equations S-20 and S-21 in Supplementary Materials). Transfer coefficients of 0.5 were employed.

An adsorption step is involved in concerted and non-concerted mechanisms and must be controlled kinetically to discriminate between the two mechanisms. The dimensionless parameter, λ_{des}^i,

represented the desorption rate constant normalized against the inverse of the time scale for the cycle of the substrate potential as given by

$$\lambda_{\mathrm{des}}^{\mathrm{i}} = k_{\mathrm{des}}^{\mathrm{i}} \frac{RT}{Fv} \tag{9}$$

This parameter is equivalent to the ratio of the normalized adsorption rate constant, $\lambda_{\mathrm{ads}}^{\mathrm{i}}$, to the normalized strength of the interactions between the adsorbate and the electrode surface, ρ_{i}, with

$$\rho_{\mathrm{i}} = c_0 \beta_{\mathrm{i}} \tag{10}$$

where $\lambda_{\mathrm{des}}^{\mathrm{i}} = \lambda_{\mathrm{ads}}^{\mathrm{i}}/\rho_{\mathrm{i}}$. The $\lambda_{\mathrm{ads}}^{\mathrm{i}}/\rho_{\mathrm{i}}$ ratio was employed in a previous study to obtain kinetic zone diagrams [2]. In this study, ρ_{i} was specified for each kinetic zone diagram.

The diffusion-limited tip reaction was assumed to simulate the tip current. In any operation mode, the tip current was given by

$$i_{\mathrm{T}} = -2\pi F \int_0^a r v_{\mathrm{T}}^{\mathrm{i}} dr \tag{11}$$

where the current due to oxidation has a positive sign [35] and $v_{\mathrm{T}}^{\mathrm{i}}$ is the diffusion-limited rate of the tip reaction of species i. The tip current was normalized against the tip current based on the diffusion-limited reduction of the oxidant in the bulk solution, $i_{\mathrm{T},\infty}$, as given by

$$i_{\mathrm{T},\infty} = -4xnFDc_0 a \tag{12}$$

where x is a function of RG; and n (= 1) is the number of transferred electrons. The substrate current was also simulated to agree with the CV response as obtained by using COMSOL and the finite difference method [3]. This agreement validated the tip current simulated in this work.

2.2. Negative ACET mode

2.2.1. Characteristic voltammograms

We simulated the tip current against the cycled substrate potential to yield characteristic voltammograms for the negative ACET mode. Specifically, we varied κ for the ACET reaction at the substrate to simulate the characteristic desorption peak current at the tip with $\kappa > 1$ (Figure 2A). The substrate potential was initially positive enough not to drive the ACET reaction at the substrate. The resultant tip current, i_T, went below $i_{T,\infty}$ owing to the negative feedback effect from the non-reactive substrate to yield the normalized tip current of $i_T/i_{T,\infty} = I_{NF} = 0.57$ as expcted at $d/a = 0.5$. The tip current decreased to zero during the cathodic forward scan of the substrate potential and then peaked during the reverse scan. Steady states were maintained during the forward scan because κ was large enough to continuously deplete the oxidant in the tip–substrate gap without the saturation of the substrate with the adsorbate. A finite amount of the adsorbate was reductively formed during the forward scan and oxidatively desorbed during the reverse scan to transiently peak the tip current.

Our simulation also revealed that the tip current response was controlled by the ACET reaction at the substrate not under the tip but outside of the tip. The concentration of the oxidant, O, in the tip–substrate gap was simulated at initial, switching, and peak potentials (Figures 2B–2D, respectively). At any potential, the oxidant was consumed by the diffusion-limited tip reaction and completely depleted at the substrate under the tip. The substrate reaction was not driven at the initial potential (Figure 2B), thereby generating no adsorbate on the substrate. The substrate reaction was diffusion-limited at the switching potential to deplete the oxidant at the entire surface of the substrate (Figure 2C), thereby yielding the zero tip current owing to the shielding effect [36]. The adsorbate was also formed at the exterior region of the substrate during the forward scan. The adsorbate was oxidatively desorbed during the reverse scan to transiently triple the concentration of the oxidant at the exterior surface of the substrate in comparison with c_0 (Figure 2D). The substrate-generated oxidant was transported laterally through the tip–substrate gap and detected at the tip to transiently enhance the tip current (Figure 1A).

Our simulation results demonstrated that all parameters of an ACET reaction at the substrate are determinable by employing the negative ACET mode. Characteristic voltammograms with $\kappa >> 1$ depended on the standard rate constant of the ACET reaction, k_C^0, at the substrate (Figure 3A) as evaluated by using Λ_C^O (Equation 8). As the ACET reaction became slower, forward and reverse waves shifted cathodically and anodically, respectively, as expected for reversible, quasi-reversible, and irreversible ACET reactions. The cathodic shift of the forward wave accelerated the slower reductive adsorption of the reductant at the substrate to deplete the oxidant in the tip–substrate gap, thereby lowering the tip current to zero. The anodic shift of the reverse wave accelerated the slower oxidative desorption of the reducant to yield a lower and broader desorption peak. The broadness of the reverse wave corresponded to the transfer coefficient, α. The observation of both forward and reverse waves also facilitated the determination of the formal potential, $E_C^{0'}$. The identical wave shape, however, was predicted with $\kappa >> 1$, thereby preventing the determination of Γ_s. Accordingly, κ must be lowered to ~1 to observe another characteristic voltammogram (Figure 3B), which allowed for the determination of Γ_s from Equation 7. The corresponding voltammogram was featured by a surface wave with an offset of the negative feedback current, $i_T/i_{T,\infty} = 0.57$. More specifically, the tip current was lowered initially by the negative feedback effect and then transiently by the reductive consumption of the oxidant to the adsorbed reductant at more negative potentials than $E_C^{0'}$ during the cathodic scan of the substrate potential. The dip of the tip current was completed by the saturation of the substrate with the adsorbed reductant. The adsorbate was oxidatively desorbed from the substrate during the anodic scan to yield a peak current at the tip. The voltammogram was dependent on k_C^0, $E_C^{0'}$, and α, which can be determined experimentally.

2.2.2. Experimental examples

The simulation results of the negative ACET mode were summarized in the kinetic zone diagram (Figure 4) and compared with experimental voltammograms. We found five zones in the kinetic zone diagram with various Λ_C^O and κ. Some notations of the kinetic zones followed those of the corresponding CV [2]. Specifically, D and A represent the diffusion-controlled and adsorptive behavior, respectively. Each zone covers reversible and irreversible ET kinetics, as indicated by R (or O) for reversible (or ordinary) kinetics and I for irreversible kinetics. The DON and DIN zones of the negative ACET mode were presented in Figure 3A and discriminated from the DO and DI zones of positive ACET and positive feedback modes. The SECM-based voltammograms of AR/AI zones were detailed in Figure 3B. Moreover, the tip current in the NF zone was identical to I_{NF} at any substrate potential.

The AI zone of the negative ACET mode simulated voltammograms for the underpotential deposition of hydrogen at the Pt substrate as studied at pH 4 (Figure 4 in [22]). The H^+ concentration was high enough to obtain a measurably high current based on the hydrogen evolution reaction at a Pt tip ($2H^+ + 2e \rightarrow H_2$). The tip-generated H_2 was not oxidized at the Pt substrate to yield $i_T/i_{T,\infty} < 1$ owing to the negative feedback effect. The substrate potential was scanned cathodically to drive the Volmer reaction at the substrate as

$$H^+ + M + e \rightleftharpoons H_{ads} \quad (13)$$

The tip current was lowered by the consumption of H^+ in the tip–substrate gap until the saturation of the substrate with H_{ad} to yield the characteristic dip of the tip current in the AI zone. The reverse scan transiently peaked the tip current as expected for the AI zone. The wide separation of ~0.2 V between the peak potentials corresponds to the electrochemical irreversibility of the Volmer reaction to indicate the AI zone, not the AR zone.

The DON zone of the negative ACET mode was observed for the underpotential deposition of hydrogen at the Pt substrate at pH 7.0 (Figure 7 in [21]). The concentration of H^+ was too low to observe the substantial tip current during the cathodic scan. H_{ads} on the substrate, however, was formed during the cathodic scan and desorbed during the reverse scan to yield a characteristic voltammogram of the DON zone. We confirmed that the desorption peak was attributed to the transient Volmer reaction, not only to the surface diffusion of H_{ads} on the Pt substrate [27] (see Figure S-2 in Supplementary Materials). The transition from the AI zone at pH 4 to the DON zone at pH 7 is due to larger κ with the lower concentration of H^+ in the solution. This consistency implies that H_{ads} is formed from the low concentration of H^+ at pH 7, where H_2O is usually considered as the H^+ source [21], i.e.,

$$H_2O + M + e \rightleftharpoons H_{ads} + OH^- \quad (14)$$

Equation 14 is not equivalent to the Volmer reaction in the acidic media and must be implemented in our model to identify the H^+ source from experimental voltammograms.

Interestingly, the characteristic voltammogram of the AI zone in the negative ACET mode was observed for the ACET-like formation of oxides at the Pt substrate (Figure 4 in [22]). The gross reaction of Pt oxidation is given by

$$PtO + 2H^+ + 2e \rightleftharpoons Pt + H_2O \quad (15)$$

Equation 15 is equivalent to an ACET reaction (Equation 1) when PtO and Pt are considered as an adsorption site and an adsorbate, respectively, in the presence of excess water. During the cathodic scan, H^+ was not reduced but consumed at the substrate to demonstrate the characteristic dip of the tip current based on the hydrogen evolution reaction. The subsequent oxidation of Pt during the anodic scan generated H^+ to peak the tip current. The reverse peak of the tip current was broadened to mirror the broadened peak of the substrate current based on the Pt oxidation.

The voltammogram of the DIN zone in the ACET mode is also similar to an experimental voltammetric plot obtained for Li electrointercalation at the graphite electrode [28]. In this case, the potential of a Hg-film-coated Pt tip was cycled to uptake and strip Li^+ during potentiostatic Li electrointercalation at the substrate. A plot of the stripping peak current against the substrate potential resembled the characteristic voltammogram of the DIN zone. The standard rate constant of Li electrointercalation was determined from not the plot of the tip current versus the substrate potential but tip stripping voltammograms at various substrate potentials. The latter analysis, however, required the kinetics of Li amalgamation at the tip, which is simplified to a diffusion limit in the ACET mode.

2.2.3. Concerted and non-concerted mechanisms

We predict that the concerted and non-concerted mechanisms of the negative ACET mode are discriminable when the adsorption of the oxidant is kinetically controlled [2, 3]. Specifically, we developed kinetic zone diagrams for concerted and non-concerted mechanisms by varying $\lambda_{\mathrm{des}}^{\mathrm{O}}$ and κ for the common adsorption step (Figures 5A and 5B, respectively). In the notation, Kin represents a forward (or reverse) wave controlled purely by adsorption (or desorption) kinetics. The weak adsorption of the oxidant with $\rho_{\mathrm{O}} = 10^{-4}$ was assumed to avoid interference with the reductant adsorption. Both concerted and non-concerted mechanisms were significantly affected by the weak oxidant adsorption to yield KinR/KinI zones in addition to DON/DIN and AR/AI zones. KinDR/KinDI zones were predicted only for the concerted mechanism. The KinDR/KinDI zones of the negative ACET mode have not been predicted theoretically or demonstrated experimentally. The characteristic voltammograms of KinR/KinI zones have not been predicted theoretically but were observed experimentally for the redox reaction of a conducting polymer film [32] as discussed below.

The kinetic zone diagrams of concerted and non-concerted mechanisms confirmed that different voltammograms are expected for the two mechanisms when the common adsorption step is kinetically controlled. Specifically, the same combination of adsorption parameters, $\lambda_{\mathrm{des}}^{\mathrm{o}}$ and κ, yielded distinct voltammograms for the two mechanisms when $\lambda_{\mathrm{des}}^{\mathrm{o}}$ is sufficiently small (Figure 5A and 5B, respectively). With $\kappa > 0.1$, the negative feedback response was predicted for the non-concerted mechanism when the adsorption step was too slow to mediate the following inner-sphere ET step (the inset of Figure 5B). With any κ in the concerted mechanism, the tip current was affected by the ACET step, which was separated from the adsorption step (the inset of Figure 5A). Uniquely, the concerted mechanism yielded the KinDR/KinDI zone, where the desorption peak was observed in contrast to the KinDR/KinDI zone and enhanced much more than in the DON/DIN zone. The high desorption peak is attributed to the slow adsorption of the oxidant, which is competitively reduced at the tip to enhance the tip current (the inset of Figure 5A).

2.2.4. ET coupled with ion transfer

We found that the characteristic voltammograms of the negative ACET mode resemble those observed experimentally for the redox reaction of a conducting polymer coupled with ion transfer. The KinI zone of the negative ACET mode simulated the SECM-based voltammogram of a poly(3,4-ethylenedioxythiophene) (PEDOT) film coupled with the transfer of an anion, X^-, (Figure 4 in [32]) as

$$PEDOT^+X^- + e \rightleftharpoons PEDOT + X^- \quad (16)$$

Equation 16 is equivalent to the ACET reaction of an adsorbed oxidant as given by

$$O_{ads} + e \rightleftharpoons M + R \quad (17)$$

where $O_{ads} = PEDOT^+X^-$, M = PEDOT, and $R = X^-$. Experimentally, the anion was detected at the tip to yield a soluble product (e.g., $2Cl^- \rightleftharpoons Cl_2 + 2e$). The tip-generated species was not reactive at the PEDOT

film to lower the tip current as expected for the negative ACET mode. The experimental voltammogram at a slow scan rate of 10 mV/s was sigmoidal with hysteresis as expected for the KinI zone. The KinI zone requires an adsorption step (compare Figures 4 and 5), which is equivalent to anion transfer as given by

$$PEDOT^+X^- \rightleftharpoons PEDOT^+ + X^- \quad (18)$$

The anion-transfer step is separated in the non-concerted mechanism from an ET step as defined by

$$PEDOT^+ + e \rightleftharpoons PEDOT \quad (19)$$

The two mechanisms are discriminable when the ion transfer step is kinetically controlled at faster scan rates to observe KinDI or NF zones (Figure 5).

The AI and DIN zones of the negative ACET mode were also observed for the redox reaction of a conducting polymer film coupled with ion transfer. The AI zone was observed for the redox reaction of a polyaniline film coupled with H^+ transfer at 5 mV/s (Figure 3a in [29]). Moreover, the DIN zone was observed for redox-coupled cation transfer at the polypyrrole film at 10 mV/s (Figure 3B in [31]). Overall, the variation of kinetic zones among AI, DIN, and KinI zones corresponds to the variation of κ, where Γ_s is determined by the availability of the redox site in the polymer films. AI, DIN, and KinI zones are common between concerted and non-concerted mechanisms, thereby indicating that the fast ion-transfer step is coupled with the rate-determining ET step (Equation 16 or 19).

2.2.5. Diffusion-limited tip reaction

The negative ACET mode employs the diffusion-limited ACET reaction at the tip, which is significantly covered with irreversible adsorbates as simulated by using our model (see Figure S-3 in Supplementary Materials). The saturation of the tip surface with irreversible adsorbates must be prevented experimentally to maintain the diffusion-limited ACET reaction at the tip. For instance,

adsorbates can be electrochemically extracted into a liquid-based tip, e.g., a tip based on a Hg film [28, 37] or an immiscible electrolyte solution [38]. The diffusion of the extracted species in the bulk liquid phase is more efficient than the surface diffusion of adsorbates [28], which also lowers the surface concentration of the adsorbates (Figure S-3). The availability of adsorption sites on the tip surface can be enhanced by roughening the tip surface [39]. A lower concentration of the oxidant (i.e., lower κ) in the solution can minimize the surface concentration of the adsorbate. The oxidant concentration, however, can not be lower than the threshold concentration of $\kappa \sim 10^4$, which is required to obtain a measurable tip current (see Equation S-27 in Supplementary Materials). Alternatively, the tip reaction can be mediated by the electrodeposition of the bulk material.

It should be noted that the ACET reaction at the tip may be mediated through the concerted or non-concerted mechanism. In the non-concerted mechanism, the preceding adsorption of the oxidant at the tip must be fast enough to reach a diffusion limit. Otherwise, the adsorption kinetics limits the tip reaction as exemplified by the NF zone of the non-concerted mechanism at the substrate (Figure 5B). In this case, the concerted mechanism will prevail to reach a diffusion limit with $\kappa > 0.1$ as ensured for the concerted mechanism at the substrate (Figure 5A).

2.3. Positive ACET mode

2.3.1. Characteristic voltammograms

We also simulated the characteristic voltammograms of the positive ACET mode, where the reductant was reversibly adsorbed both on the tip and the substrate (the inset of Figure 6A). We considered an adsorption equilibrium constant of $\rho_R = 10^5$, which corresponded to weak adsorption with a free energy change of –28.5 kJ/mol (= $-RT\ln\rho_R$ at 298 K). The weak and reversible adsorbate, however, can still saturate the electrode surface [3]. Our simulation yielded the characteristic desorption

peak of the positive ACET mode with $\kappa >> 1$ (Figure 6A). The tip current at the initial substrate potential was enhanced by the positive feedback effect from the substrate to yield the normalized tip current of $i_T/i_{T,\infty} = I_{PF} = 2.3$ as expcted at $d/a = 0.5$. The reductant was generated at the tip, adsorbed on the substrate under the tip, and oxidized through the ACET step to locally regenerate the oxidant (Figure 6B). The substrate-regenerated oxidant was reduced at the tip to enhance the tip current. As the substrate potential was scanned cathodically, the oxidant was reduced at the entire substrate (Figure 6C at the switching potential). The substrate reaction not only lowered the tip current to zero but also accumulated the reductant adsorbed on the substrate. During the anodic scan, the adsorbate was oxidatively desorbed from the substrate under the tip to transiently peak the tip current (Figure 6D), where the concentration of the oxidant at the substrate under the tip was tripled in comparison with c_0.

The voltammograms of the positive ACET mode with a characteristic desorption peak were obtained with $\kappa >> 1$ and dependent on k_C^0, $E_C^{0\prime}$, and α. The desorption peak was not only shifted anodically but also enhanced as the ACET reaction at the substrate became slower (Figure 7A). With the correspondingly lower k_C^0, the tip-generated reductant was adsorbed on the substrate but was not oxidized quickly through the ACET reaction. Subsequently, the tip current decreased from I_{PF} to I_{NF} during the cathodic scan (blue and magenta solid lines). Eventually, the tip current dropped to zero at more negative potentials owing to the shielding effect [36]. As the substrate potential was scanned anodically, the adsorbed reductant was oxidatively desorbed at more positive potentials through the ACET reaction with lower k_C^0. Since the adsorbate was formed for a longer time, the resultant desorption peak was enhanced.

In addition, characteristic voltammograms with both adsorption and desorption peaks were predicted for the positive ACET mode with $0.01 << \kappa << 10$ (Figure 7B). The tip current was initially

enhanced by the positive feedback effect and lowered transiently around $E_C^{0\prime}$ during the cathodic scan of the substrate potential. The dip of the tip current was completed by the saturation of the substrate with the adsorbed reductant. The oxidant was depleted from the tip–substrate gap at negative potentials to yield the zero tip current owing to the shielding effect [36]. The adsorbate was oxidatively desorbed from the substrate during the anodic scan to yield a peak current at the tip. The resultant voltammogram was sensitive to k_C^0 (i.e., Λ_C^O), $E_C^{0\prime}$, and α, which can be determined experimentally. The shape of voltammograms dramatically changed between $\kappa = 1$ and 10, which can be achieved experimentally by adjusting c_0 to determine Γ_s from κ.

2.3.2. Concerted and non-concerted mechanisms

The voltammograms of the positive ACET mode were simulated for various combinations of κ and λ_{des}^O and compared with those of the positive feedback mode (Figures 8A and 8B, respectively). The zone notations of A, D, Kin, R, O, I, N, and NF are the same as those defined for the negative ACET mode. In addition, DM and DP indicate the modified- and pure-diffusion-controlled zones, respectively, in the DMR/DMI, ADMR/ADMI, DPR/DPI, and ADPR/ADPI zones as defined for CV [2, 3]. The voltammograms of DO/DI and ADMR/ADMI zones were detailed for the positive ACET mode in Figures 7A and 7B, respectively. Moreover, DON/DIN, AR/AI, and NF zones were predicted for the positive ACET mode when the adsorption step was too slow to drive the ACET reaction at the substrate. The adsorption step was kinetically limited also in the DO′/DI′ zone to yield a tip current that was intermediate between DO/DI and DON/DIN zones. In the DMR/DMI zones, the adsorbates on the substrate were abundant and able to mediate the ACET reaction at the substrate but not to yield substantial peak current at the tip.

The positive ACET mode based on the concerted mechanism was compared with the positive feedback mode of the non-concerted mechanism with the same combinations of κ and $\lambda_{\mathrm{des}}^{\mathrm{O}}$ to discriminate between the two mechanisms. The voltammograms simulated for the positive feedback mode were represented by the kinetic diagram (Figure 8B) to yield the same voltammograms as the positive ACET mode in the DO/DI zone. Moreover, the ADPR and DPR zones of the positive feedback mode were thermodynamically equivalent to the DMR and ADMR zones of the positive ACET mode when both ET and adsorption steps maintained equilibrium. The thermodynamic equivalence, however, was not maintained when outer-sphere ET and ACET steps were kinetically controlled in ADPI and DPI zones and DMI and ADMI zones, respectively. The two mechanisms were distinguishable from each other despite the fast adsorption step in these zones, where the surface coverage of the substrate with the adsorbate was high [3]. The thermodynamic equivalence was not maintained when the adsorption step was kinetically controlled to yield NF and DPR/DPI zones in positive ACET and positive feedback modes, respectively. When the adsorption step was kinetically controlled, the positive feedback mode yielded AIDPR/AIDPI, DRKin/DIKin, and DRAI/DIAI zones in contrast to AR/AI, DON/DIN, and DO′/DI′ zones of the positive ACET mode.

2.3.3. Experimental identification of the ACET mechanism

We applied simulation results to discuss the mechanisms of the ACET reaction at the substrate as studied by SECM previously. We confirmed the concerted mechanism expected for the hydrogen oxidation reaction at the Pt substrate [23], where SECM-based voltammetry resulted in the ADMI zone not the AIDPI zone. The concerted mechanism corresponded to the Volmer reaction as an ACET reaction coupled with the Tafel reaction as an adsorption step ($H_2 + 2M \rightleftharpoons 2H_{ads}$). The non-concerted mechanism was prohibited because H^+ can not be reduced directly to H_2 through the outer-sphere ET

step. Experimentally, the amperometric response of a Pt tip was based on the hydrogen evolution reaction and enhanced by the oxidation of the tip-generated H_2 at the Pt substrate. The experimental voltammogram (Figure 8B in [23]) resembled the theoretical voltammogram of the ADMI zone. Specifically, the tip current was lowered by competitively reducing H^+ at the substrate during the cathodic forward scan of the substrate potential. The tip current during the reverse scan was peaked by the oxidative desorption of H_{ads} deposited during the forward scan and crossed during the reverse scan as expected for the ADMI zone. This kinetic zone is characteristic of the concerted mechanism to exclude the non-concerted mechanism. Our model, however, must be extended to determine whether the hydrogen oxidation reaction was coupled with the Tafel reaction or the Heyrovsky reaction ($H_{ads} + H^+ + e \rightleftharpoons H_2 + M$).

The kinetic zone diagrams of positive ACET and positive feedback modes were also used to confirm the non-concerted ACET reaction of ferrocene derivatives adsorbed on highly oriented pyrolytic graphite (HOPG) [27]. In this case, the characteristic voltammogram of the DRKin zone was observed when ferrocene derivatives were oxidized on the HOPG substrate to detect the ferroceniums at the tip, i.e., the SG/TC mode. Experimental voltammograms were obtained at fast scan rates of ~10 V/s and a short distance of ~50 nm with a 1 μm-diameter Pt tip to kinetically control the adsorption step. The experimental voltammograms fitted the DRKin zone of the non-concerted mechanism not the corresponding DO zone of the concerted mechanism. The observation of the DRKin zone also confirmed that reversible quasi-steady-state voltammograms at slower scan rates [40, 41] were attributed to the DPR zone, not to the DMR zone. The adsorption of ferrocene derivatives on HOPG was too weak (i.e., $\rho_R = 10$) to yield ADPR/ADPI or AIDPR/AIDPI zones (see Figure S-4 in Supplementary Materials).

It should be noted that the non-concerted mechanism of the positive feedback mode was assumed for the electrodeposition of magnetite [42]. Experimental voltammograms fitted the voltammograms simulated for the DRKin/DIKin zone (Figure 3A in [42]) but were not assessed by considering the concerted mechanism, thereby leaving ambiguity in the ACET mechanism. Moreover, magnetite electrodeposition involved a slow chemical step, which can hamper the identification of the ACET mechanism [3].

2.3.4. SG/TC mode of concerted and non-concerted mechanisms

We also simulated the SG/TC mode to discriminate between concerted and non-concerted mechanisms when the reductant was reversibly adsorbed on the substrate (Figures 9A and 9B, respectively). In either mechanism, the tip current was based on the diffusion-limited oxidation of the reductant generated at the substrate. The voltammogram of the DMR zone was identical to that of the DPR zone owing to the thermodynamic equivalence between concerted and non-concerted mechanisms. The thermodynamic equivalence was not maintained when ET steps were kinetically controlled to yield distinct voltammograms in DMI and DPI zones. Moreover, the adsorption step was kinetically controlled with low $\lambda_{\mathrm{des}}^{\mathrm{o}}$ to discriminate between the two mechanisms. The tip current was negligible for the concerted mechanism, where the slow adsorption step followed the ACET reaction to serve as the rate-determining step. By contrast, DPR/DPI zones were predicted for the non-concerted mechanism, where the reductant was generated directly through the outer-sphere ET step separated from the slow adsorption step. In addition, the concentration of the reducant must be high enough (i.e., $\kappa < 1$ in Figure 9) to obtain the significant tip current for the concerted mechanism. With $\kappa > 1$ in the non-concerted mechanism, the adsorption step can be slow enough to detect a large fraction of the substrate-generated reducant at the tip.

The experimental voltammograms measured in the SG/TC mode deviated from the simulated voltammograms when the experimental mechanism was not identical to the simulated mechanism. Magnetite electrodeposition was studied by employing the SG/TC mode to yield a peak-shaped voltammogram (Figure 3B in [42]), which can not be expected from the concerted or non-concerted mechanism without a surface chemical reaction (Figure 9). Moreover, the characteristic voltammogram of the DI zone was observed for copper electrodeposition in the SG/TC mode (Figure 4b in [33]). Experimentally, Cu^{+} was generated voltammetrically from Cu^{2+} at the glassy carbon substrate and oxidized amperometrically to Cu^{2+} at the Pt tip in the SG/TC mode. The tip current was lowered as the substrate potential was scanned cathodically to electrodeposit Cu from Cu^{+} through the ACET step on the substrate. The reverse scan of the substrate potential oxidatively desorbed Cu^{+} from Cu to peak the tip current. In the resultant voltammogram, the tip current crossed between forward and reverse scans as expected for the DI zone to indicate that the ACET step was kinetically controlled. More work is needed to assess whether the ACET step was mediated through the concerted mechanism or the non-concerted mechanism as predicted theoretically [43].

2.3.5. Diffusion-limited tip reaction

Care must be taken to drive the tip reaction at the diffusion-limited rate even when the tip is covered with reversible adsorbates. In positive ACET and positive feedback modes, the tip reduces the oxidant in the solution to the reversibly adsorbed reductant. This reaction can not reach a diffusion limit when the adsorption step is fast and the oxidant concentration is low as represented by the NR zone for both concerted and non-concerted mechanisms (Figure 9). In this case, the diffusion-limited tip reaction requires a higher concentration of the oxidant in the solution to lower κ. In the SG/TC mode, the tip reaction is the oxidation of the reductant generated at the substrate. This reaction can always reach a

diffusion limit through the non-concerted mechanism (Figure 8B) but not the concerted mechanism when the adsorption step is as slow as that in NF, AR/AI, DON/DIN, and DO′/DI′ zones (Figure 8B).

2.4. Comparison with SI Mode

Finally, we propose the ACET mode as the powerful complement of the SI mode, which has been widely used to investigate the ACET reactions at the substrate. The SI mode has been applied to quantify hydrogen adsorbates [44, 45], oxygen-containing metal electrocatalysts [46], and photoelectrochemical surface intermediates [47] as preformed through ACET or ACET-like reactions on the substrate. This work predicted that both reactions can be studied also by employing the ACET mode. In comparison with the SI mode, the ACET mode offers a few advantages and disadvantages. Advantageously, the dynamics of the ACET reaction can be investigated by the ACET mode but not by the SI mode. Moreover, a large substrate can be investigated by the ACET mode in contrast to the SI mode, which requires the tip and the substrate with similar sizes. Furthermore, a redox titrant in the solution is needed for the SI mode but not for the ACET mode. The amperometric tip current of the ACET mode is free from capacitive current in contrast to the voltammetric tip current of the SI mode. Disadvantageously, the oxidant concentration, c_0, must be low enough for the ACET mode (e.g., $\kappa > 0.1$ in Figures 4 and 5) but not for the SI mode. Moreover, the tip surface can be saturated with irreversible adsorbate in the negative ACET mode, not in the SI mode, which uses non-adsorbing and soluble redox couples as titrants. It should be noted that the reaction of an intermediate adsorbate formed through an ACET reaction, e.g., hydrogen electrocatalysis, can be studied dynamically by both SI [48, 49] and positive ACET [23] modes.

3. Conclusions

In this work, we generalized the theory of SECM-based voltammetry [25] to quantitatively understand the dynamics and mechanism of ACET reactions at the substrate. An ACET reaction can be mediated through concerted and non-concerted mechanisms when the reactant or the product is reversibly adsorbed on the substrate [3, 24]. We simulated the transient voltammograms of negative and positive ACET, positive feedback, and SG/TC modes to confirm that the ACET mechanism can be identified when the adsorption step is kinetically controlled [2, 3]. We envision that transient SECM-based voltammetry will be useful as the powerful complement of the SI mode to experimentally and quantitatively investigate actual ACET reactions. The negative ACET mode can be used to interrogate electrodeposition and electrointercalation as well as the ACET-like formation of metal oxides as electrocatalysts and the redox reaction of a conducting polymer concerted or non-concerted with ion transfer. The ACET reactions involved in electrocatalysis and photoelectrocatalysis can be studied by detecting reversible adsorbates in positive ACET and positive feedback modes as complemented by the SG/TC mode. The new theoretical framework reported in this work will facilitate the broad application of transient SECM-based voltammetry to deepen our understanding of important electrode reactions.

4. Acknowledgment

This study was supported by the National Science Foundation (grant number CHE-1904258 for S.A.). K.C.L. acknowledges funding from the Army Research Office under award ARO: W911NF-22-1-0293. D.C.J. and M.P. acknowledge the Arts and Sciences Fellowships from the University of Pittsburgh. K.B. was partially supported by the DISHA fellowship from the Department of Science and Technology, India.

5. References

[1] A.J. Bard, Inner-Sphere Heterogeneous Electrode Reactions. Electrocatalysis and Photocatalysis: The Challenge, J. Am. Chem. Soc., 132 (2010) 7559–7567.

[2] O.V. Klymenko, I. Svir, C. Amatore, Molecular Electrochemistry and Electrocatalysis: A Dynamic View, Mol. Phys., 112 (2014) 1273–1283.

[3] D.C. Janda, K. Barma, N. Kurapati, O.V. Klymenko, A. Oleinick, I. Svir, C. Amatore, S. Amemiya, Systematic Assessment of Adsorption-Coupled Electron Transfer toward Voltammetric Discrimination between Concerted and Non-Concerted Mechanisms, Electrochim. Acta, 428 (2022) 140912.

[4] E. Herrero, L.J. Buller, H.D. Abruña, Underpotential Deposition at Single Crystal Surfaces of Au, Pt, Ag and Other Materials, Chem. Rev., 101 (2001) 1897–1930.

[5] M.S. Whittingham, Lithium Batteries and Cathode Materials, Chem. Rev., 104 (2004) 4271–4302.

[6] Z.W. Seh, J. Kibsgaard, C.F. Dickens, I.B. Chorkendorff, J.K. Norskov, T.F. Jaramillo, Combining Theory and Experiment in Electrocatalysis: Insights into Materials Design, Science, 355 (2017) eaad4998.

[7] D.T. Jantz, K.C. Leonard, Characterizing Electrocatalysts with Scanning Electrochemical Microscopy, Ind. Eng. Chem. Res., 57 (2018) 7431–7440.

[8] M.-H. Shao, P. Liu, R.R. Adzic, Superoxide Anion is the Intermediate in the Oxygen Reduction Reaction on Platinum Electrodes, J. Am. Chem. Soc., 128 (2006) 7408–7409.

[9] C. Zhang, F.-R.F. Fan, A.J. Bard, Electrochemistry of Oxygen in Concentrated NaOH Solutions: Solubility, Diffusion Coefficients, and Superoxide Formation, J. Am. Chem. Soc., 131 (2009) 177–181.

[10] Y. Hori, H. Wakebe, T. Tsukamoto, O. Koga, Electrocatalytic Process of CO Selectivity in Electrochemical Reduction of CO_2 at Metal Electrodes in Aqueous Media, Electrochim. Acta, 39 (1994) 1833–1839.

[11] Y. Hori, Electrochemical CO_2 Reduction on Metal Electrodes, in: C.G. Vayenas, R.E. White, M.E. Gamboa-Aldeco (Eds.) Modern Aspects of Electrochemistry, Springer New York, New York, NY, 2008, pp. 89–189.

[12] H.H. Yang, R.L. McCreery, Elucidation of the Mechanism of Dioxygen Reduction on Metal-Free Carbon Electrodes, J. Electrochem. Soc., 147 (2000) 3420–3428.

[13] A. Ignaczak, E. Santos, W. Schmickler, Oxygen Reduction Reaction on Gold in Alkaline Solutions – The Inner or Outer Sphere Mechanisms in the Light of Recent Achievements, Curr. Opin. Electrochem., 14 (2019) 180–185.

[14] I.V. Chernyshova, P. Somasundaran, S. Ponnurangam, On the Origin of the Elusive First Intermediate of CO_2 Electroreduction, Proc. Natl. Acad. Sci. U.S.A., 115 (2018) E9261–E9270.

[15] T. Kai, M. Zhou, Z. Duan, G.A. Henkelman, A.J. Bard, Detection of $CO_2^{\bullet-}$ in the Electrochemical Reduction of Carbon Dioxide in *N*,*N*-Dimethylformamide by Scanning Electrochemical Microscopy, J. Am. Chem. Soc., 139 (2017) 18552–18557.

[16] M. Sluyters-Rehbach, J.H. Sluyters, Some Basic Views on the Influence of Reactant Adsorption on Wave Shapes in D.C., A.C. and Linear Sweep Voltammetry, J. Electroanal. Chem. and Interfacial Electrochem., 65 (1975) 831–841.

[17] L. Chen, W. Guo, Z. Xuan, S. Bi, Cyclic Reciprocal Derivative Chronopotentiometric Behavior of Electrode Process in the Presence of Adsorptive Reactants: A Theoretical Study of the Electrolysis Sequence of Adsorptive and Diffusing Electroactive Reactants, Electrochim. Acta, 55 (2010) 9051–9059.

[18] N. Kurapati, R.M. Buoro, S. Amemiya, Perspective—Beyond the Century-Long Paradigm of Hydrogen Electrochemistry through the Laviron–Amatore Paradox, J. Electrochem. Soc., 167 (2020) 146514.

[19] L.M.C. Pinto, E. Spohr, P. Quaino, E. Santos, W. Schmickler, Why Silver Deposition is so Fast: Solving the Enigma of Metal Deposition, Angew. Chem. Int. Ed., 52 (2013) 7883–7885.

[20] E. Santos, A. Lundin, K. Pötting, P. Quaino, W. Schmickler, Model for the Electrocatalysis of Hydrogen Evolution, Phys. Rev. B, 79 (2009) 235436.

[21] Y.-F. Yang, G. Denuault, Scanning Electrochemical Microscopy (SECM): Study of the Adsorption and Desorption of Hydrogen on Platinum Electrodes in Na_2SO_4 solution (pH = 7), J. Electroanal. Chem., 418 (1996) 99–107.

[22] Y.-F. Yang, G. Denuault, Scanning Electrochemical Microscopy (SECM) Study of pH Changes at Pt Electrode Surfaces in Na_2SO_4 solution (pH 4) under Potential Cycling Conditions, J. Chem. Soc., Faraday Trans., 92 (1996) 3791–3798.

[23] J. Zhou, Y. Zu, A.J. Bard, Scanning Electrochemical Microscopy Part 39. The Proton/Hydrogen Mediator Systm and its Application to the Study of the Electrocatalysis of Hydrogen Oxidation, J. Electroanal. Chem., 491 (2000) 22–29.

[24] N. Kurapati, D.C. Janda, R.J. Balla, S.-H. Huang, K.C. Leonard, S. Amemiya, Nanogap-Resolved Adsorption-Coupled Electron Transfer by Scanning Electrochemical Microscopy: Implications for Electrocatalysis, Anal. Chem., 94 (2022) 17956–17963.

[25] S. Amemiya, Heterogeneous Electron-Transfer Reactions, in: A.J. Bard, M.V. Mirkin (Eds.) Scanning Electrochemical Microscopy, CRC Press, Boca Raton, FL, 2022, pp. 105–126.

[26] J.H. Chang, A.J. Bard, Detection of the Sn(III) Intermediate and the Mechanism of the Sn(IV)/Sn(II) Electroreduction Reaction in Bromide Media by Cyclic Voltammetry and Scanning Electrochemical Microscopy, J. Am. Chem. Soc., 136 (2014) 311–320.

[27] M.A.B. Helu, H.L. Bonazza, J.L. Fernandez, Sensing Electroadsorption Reactions and Surface Mobility of Electroadsorbed Species by Scanning Electrochemical Induced Desorption, J. Electroanal. Chem., 775 (2016) 64–71.

[28] Z.T. Gossage, J. Hui, Y. Zeng, H. Flores-Zuleta, J. Rodríguez-López, Probing the Reversibility and Kinetics of Li^+ during SEI Formation and (De)intercalation on Edge Plane Graphite using Ion-Sensitive Scanning Electrochemical Microscopy, Chem. Sci., 10 (2019) 10749–10754.

[29] M.H.T. Frank, G. Denuault, Scanning Electrochemical Microscopy: Probing the Ingress and Egress of Protons from a Polyaniline Film, J. Electroanal. Chem., 354 (1993) 331–339.

[30] M.H.T. Frank, G. Denuault, Scanning Electrochemical Microscope (SECM) Study of the Relationship between Proton Concentration and Electronic Charge as a Function of Ionic Strength during the Oxidation of Polyaniline, J. Electroanal. Chem., 379 (1994) 399–406.

[31] M. Arca, M.V. Mirkin, A.J. Bard, Polymer Films on Electrodes. 26. Study of Ion Transport and Electron Transport at Polypyrrole Films by Scanning Electrochemical Microscopy, J. Phys. Chem., 99 (1995) 5040–5050.

[32] N.J. Yang, C.G. Zoski, Polymer Films on Electrodes: Investigation of Ion Transport at Poly(3,4-ethylenedioxythiophene) Films by Scanning Electrochemical Microscopy, Langmuir, 22 (2006) 10338–10347.

[33] A.P. O'Mullane, A.K. Neufeld, A.M. Bond, Monitoring Cuprous Ion Transport by Scanning Electrochemical Microscopy during the Course of Copper Electrodeposition, J. Electrochem. Soc., 155 (2008) D538–D541.

[34] J. Rodríguez-López, Surface Interrogation Mode of Scanning Electrochemical Microscopy (SI-SECM): An Approach to the Study of Adsorption and (Electro)Catalysis at Electrodes, in: A.J. Bard, C. Zoski (Eds.) Electroanalytical Chemistry: A Series of Advances, Vol 24, Crc Press-Taylor & Francis Group, Boca Raton, 2012, pp. 287–351.

[35] J.M. Pingarrón, J. Labuda, J. Barek, C.M.A. Brett, M.F. Camões, M. Fojta, D.B. Hibbert, Terminology of Electrochemical Methods of Analysis (IUPAC Recommendations 2019), Pure Appl. Chem., 92 (2020) 641–-694.

[36] C.G. Zoski, J.C. Aguilar, A.J. Bard, Scanning Electrochemical Microscopy. 46. Shielding Effects on Reversible and Quasireversible Reactions, Anal. Chem., 75 (2003) 2959–2966.

[37] M.A. Alpuche-Aviles, J.E. Baur, D.O. Wipf, Imaging of Metal Ion Dissolution and Electrodeposition by Anodic Stripping Voltammetry-Scanning Electrochemical Microscopy, Anal. Chem., 80 (2008) 3612–3621.

[38] R. Ishimatsu, A. Izadyar, B. Kabagambe, Y. Kim, J. Kim, S. Amemiya, Electrochemical Mechanism of Ion–Ionophore Recognition at Plasticized Polymer Membrane/Water Interfaces, J. Am. Chem. Soc., 133 (2011) 16300–16308.

[39] J.H. Shim, Y. Lee, Amperometric Nitric Oxide Microsensor Based on Nanopore-Platinized Platinum: The Application for Imaging NO Concentrations, Anal. Chem., 81 (2009) 8571–8576.

[40] N. Nioradze, R. Chen, N. Kurapati, A. Khvataeva-Domanov, S. Mabic, S. Amemiya, Organic Contamination of Highly Oriented Pyrolytic Graphite As Studied by Scanning Electrochemical Microscopy, Anal. Chem., 87 (2015) 4836–4843.

[41] R. Chen, R.J. Balla, Z.T. Li, H.T. Liu, S. Amemiya, Origin of Asymmetry of Paired Nanogap Voltammograms Based on Scanning Electrochemical Microscopy: Contamination Not Adsorption, Anal. Chem., 88 (2016) 8323–8331.

[42] M.A. Bhat, N. Nioradze, J. Kim, S. Amemiya, A.J. Bard, In Situ Detection of the Adsorbed Fe(II) Intermediate and the Mechanism of Magnetite Electrodeposition by Scanning Electrochemical Microscopy, J. Am. Chem. Soc., 139 (2017) 15891–15899.

[43] L.M.C. Pinto, P. Quaino, E. Santos, W. Schmickler, On the Electrochemical Deposition and Dissolution of Divalent Metal Ions, ChemPhysChem, 15 (2014) 132–138.

[44] J. Rodríguez-López, A.J. Bard, Scanning Electrochemical Microscopy: Surface Interrogation of Adsorbed Hydrogen and the Open Circuit Catalytic Decomposition of Formic Acid at Platinum, J. Am. Chem. Soc., 132 (2010) 5121–5129.

[45] D.T. Jantz, T.E. Seuferling, K.C. Leonard, Numerical Deconvolution of Surface Interrogation Scanning Electrochemical Microscopy Experiments on Platinum During Hydrogen Evolution, ChemElectroChem, 7 (2020) 4842–4842.

[46] H.S. Ahn, A.J. Bard, Surface Interrogation Scanning Electrochemical Microscopy of $Ni_{1-x}Fe_xOOH$ ($0 < x < 0.27$) Oxygen Evolving Catalyst: Kinetics of the "Fast" Iron Sites, J. Am. Chem. Soc., 138 (2016) 313–318.

[47] M.R. Krumov, B.H. Simpson, M.J. Counihan, J. Rodríguez-López, In Situ Quantification of Surface Intermediates and Correlation to Discharge Products on Hematite Photoanodes Using a Combined Scanning Electrochemical Microscopy Approach, Anal. Chem., 90 (2018) 3050–3057.

[48] H.S. Ahn, A.J. Bard, Electrochemical Surface Interrogation of a MoS_2 Hydrogen-Evolving Catalyst: In Situ Determination of the Surface Hydride Coverage and the Hydrogen Evolution Kinetics, J. Phys. Chem. Lett., 7 (2016) 2748–2752.

[49] Z. Liang, H.S. Ahn, A.J. Bard, A Study of the Mechanism of the Hydrogen Evolution Reaction on Nickel by Surface Interrogation Scanning Electrochemical Microscopy, J. Am. Chem. Soc., 139 (2017) 4854–4858.

Figure Captions

Figure 1. Scheme of (A) negative and (B) positive ACET modes of SECM with a disk-shaped tip over a macroscopic substrate. Red, blue, and black arrows indicate ACET, adsorption, and diffusion steps, respectively. The magenta arrow indicates the ACET step coupled with the adsorption step or the outer-sphere ET step. We employed the tip inner radius of a to define the tip outer radius of $r_g = 2.0a$ and the tip–substrate distance of $d = 0.5a$ in this work.

Figure 2. (A) Characteristic voltammogram with a desorption peak simulated for the negative ACET mode with $\Lambda_C^O = 10$ and $\kappa = 10$ and the corresponding concentrations of the oxidant, O, around the tip–substrate gap at (B) initial, (C) switching, and (D) peak potentials. Solid and dashed lines correspond to forward and reverse scans of the substrate potential, respectively. Red and black arrows indicate ACET and diffusion steps, respectively.

Figure 3. Effect of the normalized standard ACET rate constant, Λ_C^O, on characteristic voltammograms of the negative ACET mode with $\kappa =$ (A) 10 or (B) 1. Solid and dashed lines correspond to forward and reverse scans of the substrate potential, respectively.

Figure 4. Kinetic zone diagram of the negative ACET mode. Reversible and irreversible voltammograms (red and black lines, respectively) of each zone are indicated by positive current and positive potential directed up and right, respectively. Solid and dashed lines correspond to forward and reverse scans of the substrate potential, respectively. Zone notations: D stands for diffusion-controlled

behavior; A for adsorptive; R (or O) for reversible (or ordinary); I for irreversible; N for the negative ACET mode; and NF for the negative feedback tip current.

Figure 5. Kinetic zone diagrams of the negative ACET mode with (A) concerted and (B) non-concerted mechanisms based on the reversible adsorption of the oxidant, O, with $\rho_O = 10^{-4}$ at the substrate. Reversible and irreversible voltammograms (red and black lines, respectively) of each zone are indicated by positive current and positive potential directed up and right, respectively. Solid and dashed lines correspond to forward and reverse scans of the substrate potential, respectively. Zone notations: D stands for diffusion-controlled behavior; A for adsorptive; R (or O) for reversible (or ordinary); I for irreversible; N for the negative ACET mode; and NF for the negative feedback tip current. Kin indicates that the forward (or reverse) wave is kinetically controlled by the adsorption (or desorption) step. Red, blue, and black arrows indicate ET, adsorption, and diffusion steps, respectively.

Figure 6. (A) Characteristic voltammogram with a desorption peak simulated for the positive ACET mode with $\Lambda_C^O = 10$ and $\kappa = 100$ and the corresponding concentrations of the oxidant, O, around the tip–substrate gap at (B) initial, (C) switching, and (D) peak potentials. Solid and dashed lines correspond to forward and reverse scans of the substrate potential, respectively. Red, blue, and black arrows indicate ACET, adsorption, and diffusion steps, respectively. The magenta arrow indicates the ACET step coupled with the adsorption step or the outer-sphere ET step.

Figure 7. Effect of the normalized standard ACET rate constant, Λ_C^O, on characteristic voltammograms of the positive ACET mode for the equilibrium adsorption of the reductant, R, with $\rho_R = 10^5$, $\lambda_{des}^O = 10^2$,

and κ = (A) 10^2 or (B) 1. Solid and dashed lines correspond to forward and reverse scans of the substrate potential, respectively.

Figure 8. Kinetic zone diagrams of (A) positive ACET and (B) positive feedback modes for concerted and non-concerted mechanisms, respectively, based on the reversible adsorption of the reductant, R, with ρ_R = 10^5 at the substrate. Reversible and irreversible voltammograms (red and black lines, respectively) of each zone are indicated by positive current and positive potential directed up and right, respectively. Solid and dashed lines correspond to forward and reverse scans of the substrate potential, respectively. Zone notations: D stands for diffusion-controlled behavior; A for adsorptive; R (or O) for reversible (or ordinary); I for irreversible; N for the negative ACET mode; and NF for the negative feedback tip current. Kin indicates that the forward (or reverse) wave is kinetically controlled by the adsorption (or desorption) step. DM and DP indicate the modified- and pure-diffusion-controlled zones, respectively. Red, blue, and black arrows indicate outer-sphere ET, adsorption, and diffusion steps, respectively. The magenta arrow indicates the ACET step coupled with the adsorption step or the outer-sphere ET step.

Figure 9. Kinetic zone diagrams of the SG/TC mode for (A) concerted and (B) non-concerted mechanisms based on the reversible adsorption of the reductant, R, with ρ_R = 10^5 at the substrate. Reversible and irreversible voltammograms (red and black lines, respectively) of each zone are indicated by negative current and negative potential directed down and left, respectively. Solid and dashed lines correspond to forward and reverse scans of the substrate potential, respectively. Zone notations: R for reversible; I for irreversible; and NR for negligible tip current. DM and DP stand for modified- and pure-diffusion-controlled, respectively. Red, blue, and black arrows indicate ET, adsorption, and

diffusion steps, respectively. The magenta arrow indicates the ACET step coupled with the adsorption step or the outer-sphere ET step.

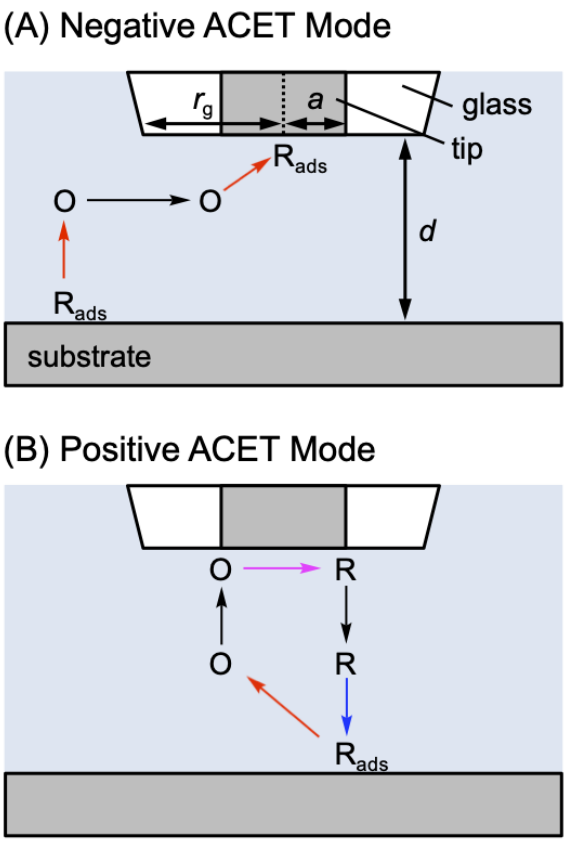
(A) Negative ACET Mode
r_g
a
glass
tip
R_{ads}
O
O
R_{ads}
d
substrate
(B) Positive ACET Mode
O
R
O
R
R_{ads}

Figure 1

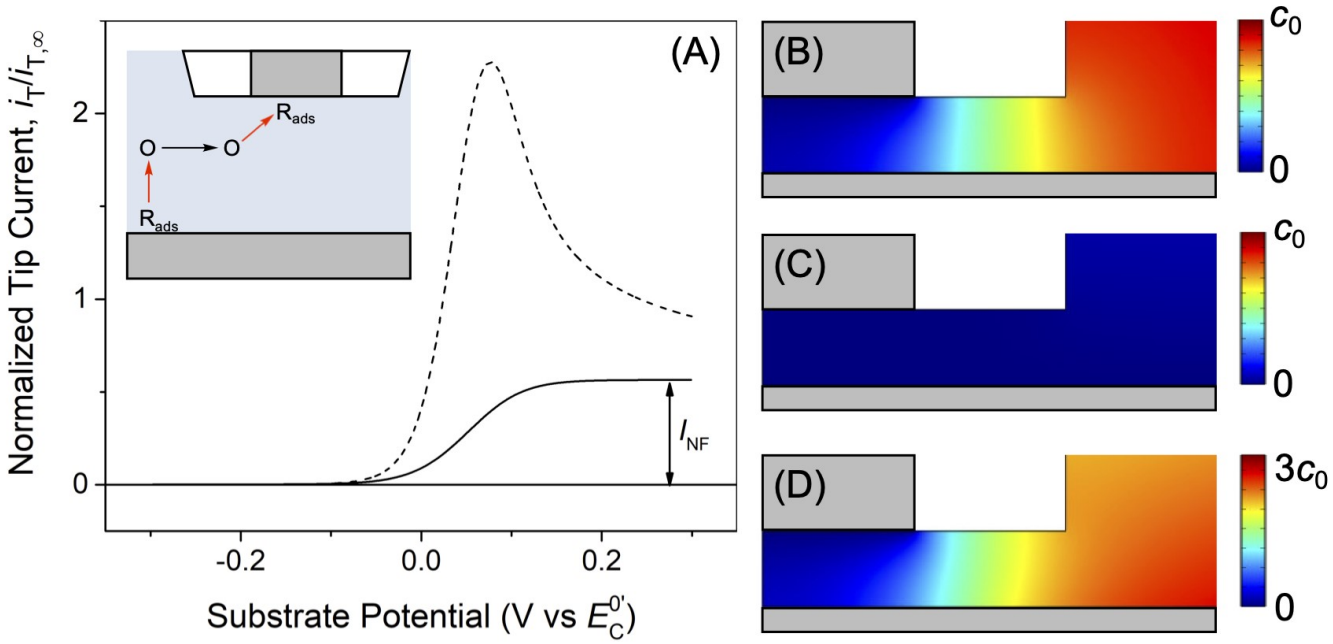
(A)
(B)
(C)
(D)
Normalized Tip Current, $i_T/i_{T,\infty}$
Substrate Potential (V vs $E_C^{0'}$)
I_{NF}
R_{ads}
O → O
c_0
$3c_0$
0
1
2
-0.2
0.0
0.2

Figure 2

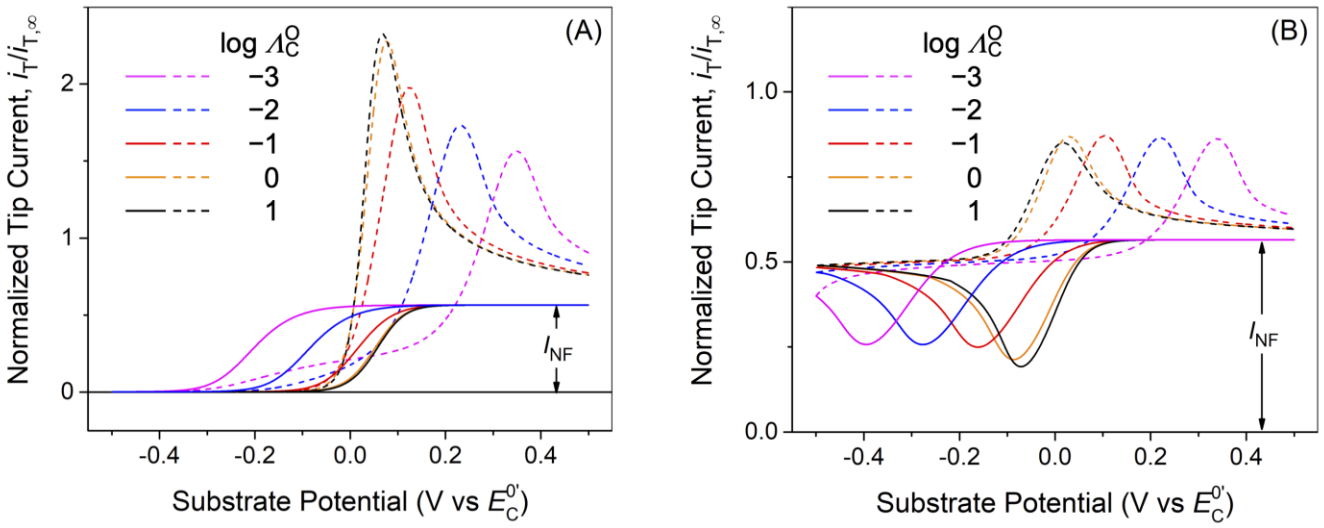
(A)
log Λ_C^O
−3
−2
−1
0
1
Normalized Tip Current, $i_T/i_{T,\infty}$
Substrate Potential (V vs $E_C^{0'}$)
I_{NF}
(B)
log Λ_C^O
−3
−2
−1
0
1
Normalized Tip Current, $i_T/i_{T,\infty}$
Substrate Potential (V vs $E_C^{0'}$)
I_{NF}

Figure 3

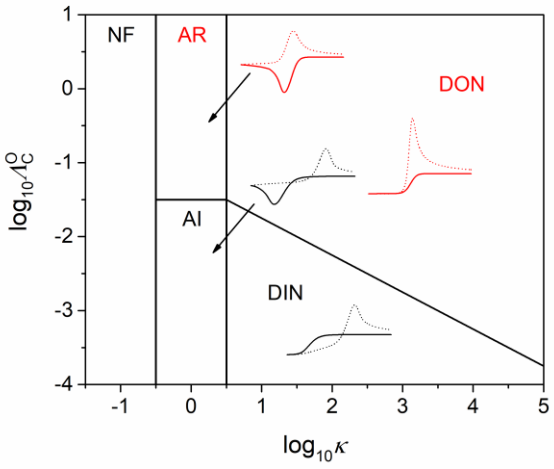

Figure 4

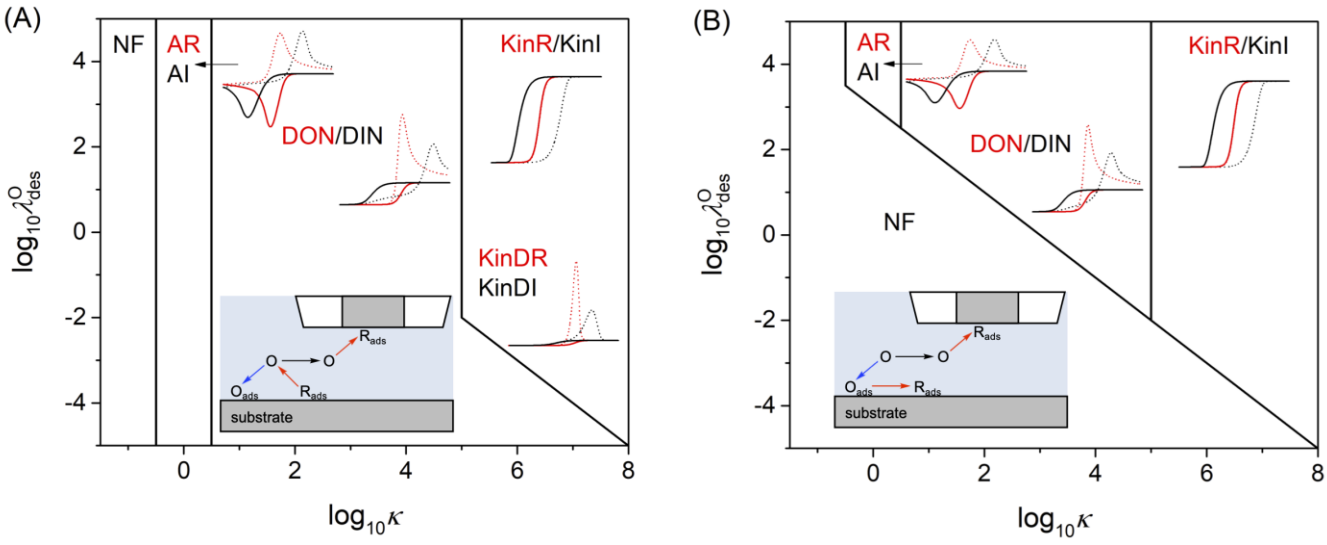
(A)
NF
AR
AI
DON/DIN
KinR/KinI
KinDR
KinDI
substrate
$\log_{10}\lambda^{O}_{des}$
$\log_{10}\kappa$
(B)
AR
AI
DON/DIN
KinR/KinI
NF
substrate
$\log_{10}\lambda^{O}_{des}$
$\log_{10}\kappa$

Figure 5

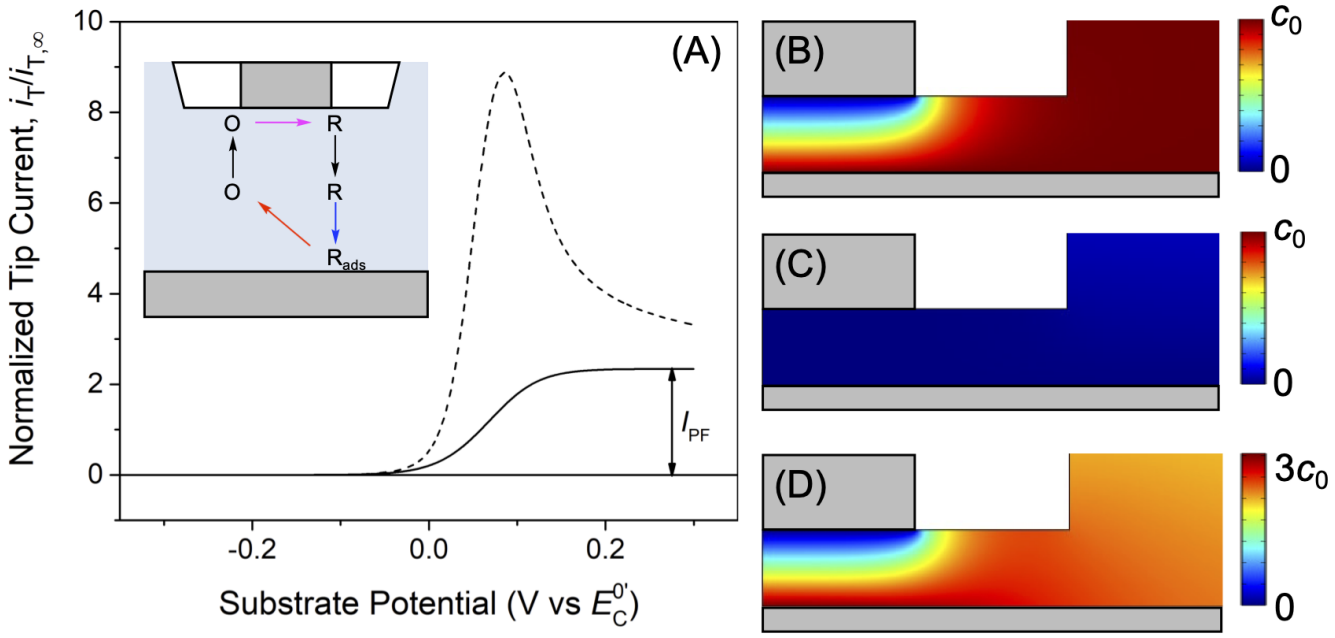
(A)
(B)
(C)
(D)
Normalized Tip Current, $i_T/i_{T,\infty}$
Substrate Potential (V vs $E_C^{0'}$)
I_{PF}
O
R
R_{ads}
c_0
0
$3c_0$

Figure 6

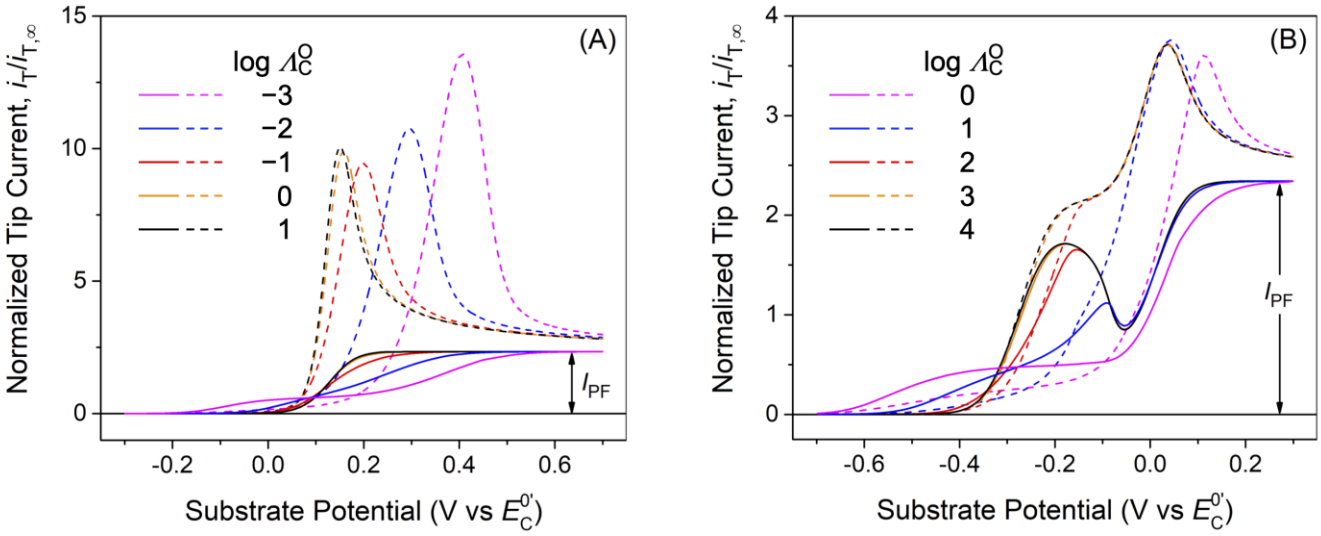
(A)
log Λ_C^O
−3
−2
−1
0
1
Normalized Tip Current, $i_T/i_{T,\infty}$
Substrate Potential (V vs $E_C^{0'}$)
I_{PF}
(B)
log Λ_C^O
0
1
2
3
4
Normalized Tip Current, $i_T/i_{T,\infty}$
Substrate Potential (V vs $E_C^{0'}$)
I_{PF}

Figure 7

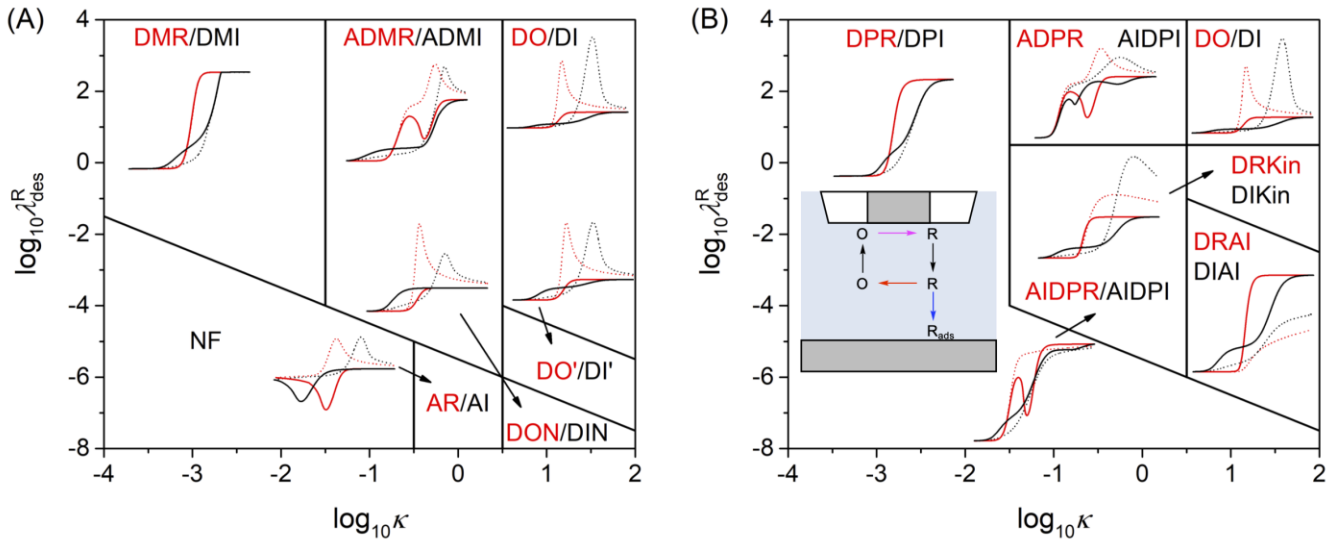
(A)
DMR/DMI
ADMR/ADMI
DO/DI
NF
AR/AI
DO'/DI'
DON/DIN
$\log_{10}\lambda^{R}_{des}$
$\log_{10}\kappa$
(B)
DPR/DPI
ADPR
AIDPI
DO/DI
DRKin
DIKin
DRAI
DIAI
AIDPR/AIDPI
O
R
R_{ads}

Figure 8

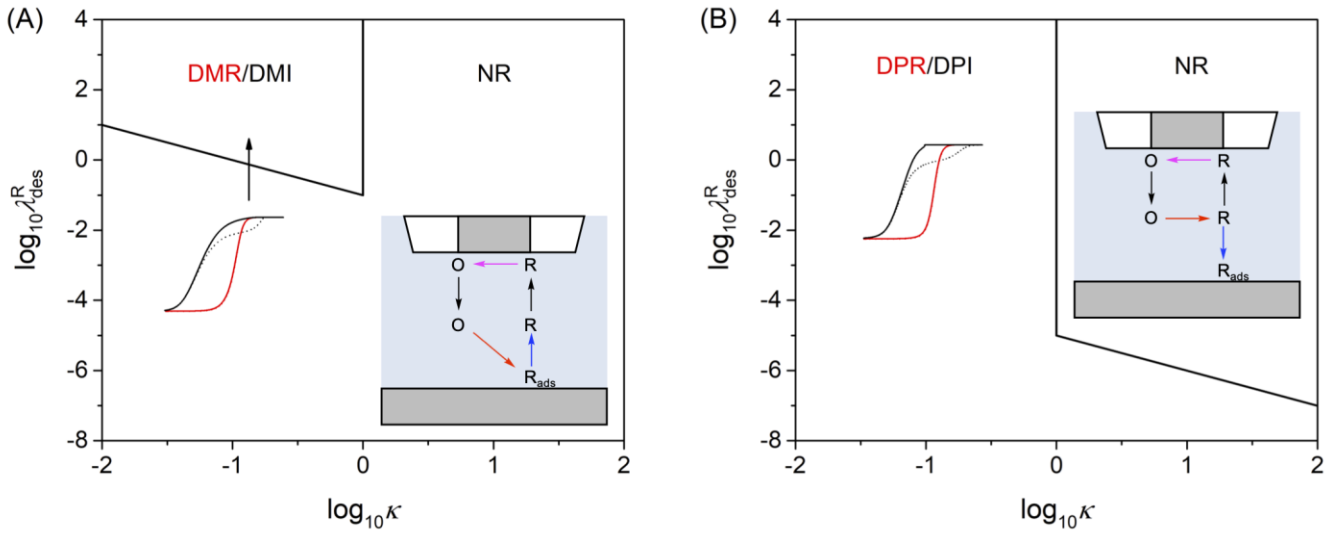
(A)
DMR/DMI
NR
O
R
O
R
R_ads
log10λ^R_des
log10κ
(B)
DPR/DPI
NR
O
R
O
R
R_ads
log10λ^R_des
log10κ

Figure 9